

Dynamics of sessile drops.

Part 3. Theory of forced oscillations

J. B. BOSTWICK^{1†} AND P. H. STEEN^{2,3}

¹Department of Mechanical Engineering, Clemson University, Clemson, SC 29631, USA

²Department of Theoretical & Applied Mechanics, Cornell University, Ithaca, NY 14853, USA

³School of Chemical and Biomolecular Engineering and Center for Applied Mathematics,
Cornell University, Ithaca, NY 14853, USA

(Received 4 November 2021)

A partially-wetting sessile drop is driven by a sinusoidal pressure field that produces capillary waves on the liquid/gas interface. The analysis presented in Part 1 of this series (Bostwick & Steen 2014) is extended by computing response diagrams and phase shifts for the viscous droplet, whose three phase contact-line moves with contact-angle that is a smooth function of the contact line speed. Viscous dissipation is incorporated through the viscous potential flow approximation and the critical Ohnesorge number bounding regions beyond which a given mode becomes over-damped is computed. Davis dissipation originating from the contact-line speed condition leads to damped oscillations for drops with finite contact-line mobility, even for inviscid fluids. The critical mobility and associated driving frequency to generate the largest Davis dissipation is computed. Lastly, regions of modal coexistence where two modes can be simultaneously excited by a single forcing frequency are identified. Predictions compare favorably to related experiments on vibrated drops.

Key Words: drops, capillary waves, contact lines

1. Introduction

Driven droplets play a critical role in a number of emerging technologies, such as 3D printing (Calvert 2001) with application to rapid prototyping (Grimm 2004), self-cleansing surfaces for enhanced solar cell efficiency (Park *et al.* 2011), microfluidics (Stone *et al.* 2004), inkjets (Castrejon-Pita *et al.* 2013; Basaran *et al.* 2013), spray cooling for high heat flux applications (Kim 2007), and drop atomization for drug delivery (aerosol) methods (Donnelly *et al.* 2004), all of which involve the motion of liquids on scales where surface tension dominates.

Forcing of sessile drops can induce shape change or drive fluid transport. Shape change occurs in experiments by driving droplets using electrowetting (Mampallil *et al.* 2013), surface acoustic waves (Baudoin *et al.* 2012), air jets (Deepu *et al.* 2014), mechanically vibrated substrates (Vukasinovic *et al.* 2007; Chang *et al.* 2013) or pressure excitations (Tilger *et al.* 2013). Bulk translational motion of driven droplets can be achieved provided contact angle hysteresis can be overcome to mobilize the three phase contact line (Noblin *et al.* 2004). Brunet *et al.* (2007) have demonstrated that a mechanically-vibrated drop can be made to walk ‘uphill’ against gravity in a ratchet-like motion

† Email address for correspondence: jbstwi@clemson.edu

(Noblin *et al.* 2009). A description of the fluid mechanical droplet response to the applied driving force is crucial in understanding the aforementioned applications, as well as guiding future studies led by prediction.

In Part 1 of this series (Bostwick & Steen 2014), we analyzed the linear stability of the sessile drop, parameterized by the static contact angle α , with a contact line that was i) pinned, ii) mobile or iii) obeyed a constitutive law that relates the contact angle to the contact line speed. The natural frequencies ω obey an operator equation

$$-\omega^2 M[y] + K[y] = 0, \quad (1.1)$$

for the disturbance shape y that takes the familiar form for a simple harmonic oscillator with M representative of fluid inertia (mass) and K the restoring force of capillarity (spring constant). Eigenmode solutions of (1.1) are characterized by the wavenumber pair $[k, l]$ that follow the spherical harmonic classification scheme (MacRobert 1967). The associated eigenfrequencies depend strongly upon the wetting properties of the solid substrate α and the mobility of the contact-line Λ . Our frequency predictions compare favorably to experiments (Sharp *et al.* 2011; Chang *et al.* 2013) and finite element simulations (Basaran & DePaoli 1994) in the appropriate limits.

In this part, we extend our analysis by introducing external forcing through the drop's bulk pressure $p = F_0 e^{i\lambda t}$ with λ the applied forcing frequency, as is the standard approach for Faraday oscillations (Benjamin & Ursell 1954). When bulk viscosity is included in the model, our forced-damped extension takes the form of a damped-driven oscillator

$$-\lambda^2 M[y] + i\lambda\epsilon C[y] + K[y] = F_0. \quad (1.2)$$

The dissipation C encompasses bulk dissipation from viscosity ϵ and Davis (1980) dissipation related to the dynamic effects associated with the contact-line speed law, as outlined in Bostwick & Steen (2015, Sec. 3.3). For reference, this condition is sometimes referred to as the Hocking condition in the literature (Hocking 1987). In Part 2 (Chang *et al.* 2015), we solved (1.2) for drops with pinned contact lines ($\Lambda = \infty$) using viscous potential flow to evaluate the dissipation C for a specific $\epsilon = 0.0024$ to compare with experiment. The focus in this part is the contact-line mobility and a comprehensive exploration of the parameter space. We solve (1.2) reporting response diagrams and phase shifts, as they depend upon the viscosity ϵ , contact angle α and contact line mobility Λ .

Lord Rayleigh (1879) showed that free drops exhibit a discrete spectrum, which has come to be referred to as the Rayleigh-Lamb (RL) spectrum (Lamb 1932). The RL spectrum has been verified experimentally for free drops (Trinh & Wang 1982; Wang *et al.* 1996) and is relevant in applications where the drop may not be completely free (Noblin *et al.* 2005; Chebel *et al.* 2011). Typical extensions for free drops include, but are not limited to, the effects of i) viscosity (Reid 1960; Chandrasekhar 1961; Miller & Scriven 1968; Prosperetti 1980), ii) large-amplitude perturbations (Tsamopoulos & Brown 1983; Lundgren & Mansour 1988) or iii) constrained geometries (Strani & Sabetta 1984; Bostwick & Steen 2009; Ramalingam & Basaran 2010; Bostwick & Steen 2013a). Recent experiments by Chang *et al.* (2013) have shown the inadequacy of the RL spectrum for partially-wetting drops ($\alpha = 75^\circ$) with pinned contact lines. The theory developed in Part 1, which accounts for the wetting properties of the solid substrate, compares favorably with these experiments.

Forced drops exhibit a finite bandwidth of forcing frequencies over which a particular mode may be excited, in contrast to the discrete (delta-function) response for unforced drops. In Part 2 of this series (Chang *et al.* 2015), observed frequency bands in experiments on mechanically-excited sessile water drops over a range of static contact angles

were reported. Viscosity tends to decrease the droplet amplitude response and increase the bandwidth for a given mode, consistent with the experiments by Sharp (2012).

Here we also include viscosity through the viscous potential flow approximation (Joseph 2006), in which the bulk dissipation is evaluated using the velocity potential. Our bandwidth predictions compare favorably against experiment over a range of contact angles (Sharp 2012). In addition, we compute the critical viscosity ϵ_c above which the oscillations for a particular mode become overdamped. This represents a bound above which a given mode cannot be harmonically excited. Our results may be viewed as a guide in designing experiments or applications where excitation of a specific mode is desirable.

Davis dissipation occurs for drops with finite contact-line mobility and leads to attenuated droplet response and increased bandwidth, even for inviscid fluids (Lyubimov *et al.* 2004, 2006). However, the scaling of Davis dissipation differs from that for bulk viscous effects. For reference, the decay rate γ from viscous dissipation for a free drop scales with the viscosity ν as $\gamma = \nu/R^2(k-1)(2k+1)$. We compute the critical mobility and forcing frequency to generate the largest Davis dissipation in order to guide future experiments. With regard to comparison against the Chang *et al.* (2015) experiments, we are able to reproduce the observed frequency envelopes only by considering effects from finite contact-line mobility, which strongly argues for treating similar problems using the contact-line speed law.

In Part 1, it was shown that spectral ordering for the sessile drop can become broken and disordered for a range of contact angles. For the forced problem with finite bandwidth, we showed that two distinct modes may be simultaneously excited by a single forcing frequency and mapped these regions of modal coexistence in parameter space for a number of modal pairs. Identifying these regions is important for 3D printing Calvert (2001), mixing (Mampallil *et al.* 2011) and drop atomization (Tsai *et al.* 2012) applications. The contact-line mobility strongly affects the size of the coexistence regions. In Part 2, we showed that mode selection in experiment is hysteretic in the coexistence regimes. That is, the dominant mode possibly depends upon the direction of the frequency sweep. Here we focus on generating ‘operating windows’ for particular droplet behavior in anticipation of future studies.

We begin this paper by deriving the governing equations for the forced droplet and show how the fluid response depends upon the wetting properties through the contact angle α , contact line mobility Λ and viscosity through the Ohnesorge number ϵ . Viscous dissipation is introduced via the viscous potential flow approximation leading to the damping of oscillations for $\epsilon < \epsilon_c$, where ϵ_c is the critical viscosity above which oscillations are overdamped for a particular mode. We then show finite contact line mobility Λ leads to Davis dissipation and compute the critical mobility Λ_m leading to the largest dissipation. Lastly, we show that two distinct modes may be simultaneously excited by a single forcing frequency and map these regions of modal coexistence in parameter space for a number of modal pairs. Comparison with relevant experiments is made when appropriate.

2. Mathematical formulation

Our derivation follows the boundary integral approach of Bostwick & Steen (2013*b*, Sec. 1) in which normal modes are invoked and the flow problem (interior domain) is mapped onto the undisturbed interface. For brevity, we follow the development set forth in Part 1 (Bostwick & Steen 2014), extending the analysis presented in Part 2 (Chang *et al.* 2015) to include the effects of contact-line mobility.

Consider an incompressible, viscous fluid subject to a time-dependent pressure field $p(t) = P_0 e^{i\Omega t}$, occupying a domain D bounded by a spherical-cap interface ∂D^f held

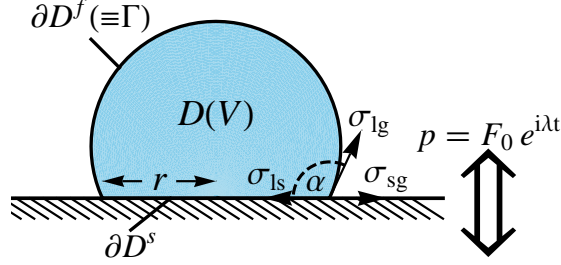


FIGURE 1. Definition sketch: spherical-cap droplet of volume V and free surface Γ with contact angle α and liquid/gas σ_{lg} , solid/gas σ_{sg} and liquid/solid σ_{ls} surface tensions, driven by an applied pressure field $p = F_0 e^{i\lambda t}$ of amplitude F_0 and frequency λ .

by a constant surface tension σ and a support surface ∂D^s , as shown in Figure 1. The equilibrium surface Γ is defined parametrically as

$$X(s, \varphi; \alpha) = \frac{\sin(s)}{\sin(\alpha)} \cos(\varphi), \quad Y(s, \varphi; \alpha) = \frac{\sin(s)}{\sin(\alpha)} \sin(\varphi), \quad Z(s; \alpha) = \frac{\cos(s) - \cos(\alpha)}{\sin(\alpha)}, \quad (2.1)$$

using arclength-like $s \in [0, \alpha]$ and azimuthal angle $\varphi \in [0, 2\pi]$ as surface coordinates, with α the static contact-angle. The interface is given a small perturbation $\eta(s, \varphi, t)$. No domain perturbation is needed for small deformations, thus the droplet domain

$$D \equiv \{(x, y, z) \mid 0 \leq x \leq X(s, \varphi; \alpha), 0 \leq y \leq Y(s, \varphi; \alpha), 0 \leq z \leq Z(s; \alpha)\} \quad (2.2)$$

is bounded by a free surface $\partial D^f (\equiv \Gamma)$ of constant surface tension σ , and a planar surface-of-support ∂D^s ;

$$\partial D^f \equiv \{(x, y, z) \mid x = X(s, \varphi; \alpha), y = Y(s, \varphi; \alpha), z = Z(s; \alpha)\}, \quad \partial D^s \equiv \{(x, y, z) \mid z = 0\}. \quad (2.3)$$

2.1. Governing hydrodynamic equations

We assume the velocity field $\mathbf{v} = -\nabla \Psi$ can be expressed using the velocity potential Ψ (Padrino *et al.* 2007), noting that this form of the velocity field cannot satisfy the no-slip condition on the solid support, but we can evaluate the bulk dissipation from the irrotational field. This assumption is the essence of viscous potential flow theory. The velocity potential Ψ satisfies the following boundary value problem,

$$\nabla^2 \Psi = 0 \quad [D], \quad \nabla \Psi \cdot \hat{\mathbf{z}} = 0 \quad [\partial D^s], \quad \frac{\partial \Psi}{\partial n} = -\frac{\partial \eta}{\partial t} \quad [\partial D^f]. \quad (2.4)$$

The pressure field p is given by the linearized Bernoulli equation

$$p = \varrho \frac{\partial \Psi}{\partial t} + P_0 e^{i\Omega t} \quad [D], \quad (2.5)$$

where ϱ is the fluid density. Finally, disturbances to the equilibrium surface Γ generate pressure gradients, and thereby flows, according to the Young-Laplace equation

$$p - \mu \hat{\mathbf{n}} \cdot (\nabla \otimes \nabla \Psi) \cdot \hat{\mathbf{n}} = -\sigma (\Delta_\Gamma \eta + (\kappa_1^2 + \kappa_2^2) \eta) \quad [\partial D^f], \quad (2.6)$$

where \otimes is the tensor product and μ the fluid viscosity. The Laplace-Beltrami operator Δ_Γ is defined on the equilibrium surface Γ and operates on functions η ,

$$\Delta_\Gamma \eta \equiv \frac{1}{\sqrt{g}} \frac{\partial}{\partial u^\mu} \left(\sqrt{g} g^{\mu\nu} \frac{\partial \eta}{\partial u^\nu} \right) \quad (2.7)$$

with the surface metric given by

$$g_{\mu\nu} \equiv \mathbf{x}_\mu \cdot \mathbf{x}_\nu = \begin{pmatrix} \csc^2(\alpha) & 0 \\ 0 & (\csc(\alpha) \sin(s))^2 \end{pmatrix}, \quad g = (\sin(s) \csc(\alpha))^2, \quad (2.8)$$

and $\mu, \nu = 1, 2$, using notation standard to differential geometry (e.g. Kreyszig 1991).

The governing equations (2.4)-(2.6) are augmented with a boundary condition on the three-phase contact-line to yield a well-posed system of partial differential equations, a condition which we discuss later.

2.2. Normal mode reduction

We assume normal modes for the interface disturbance η and velocity potential Ψ ,

$$\eta(s, \varphi, t) = y(s) e^{il\varphi} e^{i\Omega t}, \quad \Psi(\mathbf{x}, t) = \phi(\rho, \theta) e^{il\varphi} e^{i\Omega t}, \quad (2.9)$$

with l the azimuthal wavenumber and Ω the forcing frequency. The normal stress balance at the interface (2.6) can be written as

$$\sin^2(\alpha) \left(\left(\frac{\partial \phi}{\partial n} \right)'' + \cot(s) \left(\frac{\partial \phi}{\partial n} \right)' + \left(2 - \frac{l^2}{\sin^2(s)} \right) \left(\frac{\partial \phi}{\partial n} \right) \right) = \lambda^2 \phi - i\lambda \epsilon \hat{n} \cdot (\nabla \otimes \nabla \phi) \cdot \hat{n} + \lambda F_0, \quad (2.10)$$

where $\epsilon \equiv \mu / \sqrt{\rho r \sigma}$ is the Ohnesorge number, $\lambda \equiv \Omega \sqrt{\rho r^3 / \sigma}$ the scaled forcing frequency, $F_0 = P_0 r^2 / \sigma$ the scaled forcing amplitude and $' = d/ds$. The contact-line dynamics obey the general contact-line law relating the deviation in contact-angle from its static value $\Delta\alpha$ to the contact-line speed u_{CL} (Bostwick & Steen 2014, §3.2.3, Fig. 1c);

$$\frac{\partial}{\partial s} \left(\frac{\partial \phi}{\partial n} \right) + \cos(\alpha) \left(\frac{\partial \phi}{\partial n} \right) = i\lambda \Lambda \left(\frac{\partial \phi}{\partial n} \right), \quad (2.11)$$

where Λ is the contact-line mobility (Davis 1980; Hocking 1987). Note that $\Lambda = 0$ corresponds to the natural and $\Lambda = \infty$ to the pinned contact-line disturbance, respectively. The velocity potential additionally satisfies the following auxiliary conditions (Bostwick & Steen 2014, Eq. 2.13);

$$\nabla^2 \phi - \frac{l^2}{\rho^2 \sin^2 \theta} \phi = 0 \quad [D], \quad \frac{\partial \phi}{\partial n} = 0 \quad [\partial D^s], \quad \frac{\partial \phi}{\partial n} = -i\lambda y \quad [\partial D^f], \quad \int_{\Gamma} \frac{\partial \phi}{\partial n} d\Gamma = 0. \quad (2.12)$$

2.3. Derivation of integrodifferential equation

We write the solution to (2.10–2.12) as an integral equation

$$(1 - b^2) \frac{\partial \phi}{\partial n}(x) = -i\lambda \epsilon \int_b^1 G(x, y) (\hat{n} \cdot (\nabla \otimes \nabla \phi) \cdot \hat{n}) dy + \lambda^2 \int_b^1 G(x, y) \phi(y) dy + F_0 \lambda \int_b^1 G(x, y) dy, \quad (2.13)$$

using the Green's function

$$G(x, y; l, \lambda, \Lambda) = \begin{cases} \xi(l) y_1(y; l) \left[\frac{\tau_2}{\tau_1} y_1(x; l) - y_2(x; l) \right] & b < x < y < 1 \\ \xi(l) y_1(x; l) \left[\frac{\tau_2}{\tau_1} y_1(y; l) - y_2(y; l) \right] & b < y < x < 1, \end{cases} \quad (2.14)$$

where $x \equiv \cos(s)$, $b \equiv \cos(\alpha)$. The functions y_1 and y_2 belong to the kernel of the curvature operator K and are given by

$$\begin{aligned} y_1(x; 0) &= P_1(x), \quad y_2(x; 0) = Q_1(x), \quad y_1(x; 1) = P_1^{(1)}(x), \quad y_2(x; 1) = Q_1^{(1)}(x), \\ y_1(x; l \geq 2) &= (x+l) \left(\frac{1-x}{1+x} \right)^{l/2}, \quad y_2(x; l \geq 2) = \frac{(x+l)}{2l(l^2-1)} \left(\frac{1+x}{1-x} \right)^{l/2}, \end{aligned} \quad (2.15)$$

where P_1, Q_1 and $P_1^{(1)}, Q_1^{(1)}$ are the order 0 and 1 Legendre functions of index 1, respectively (MacRobert 1967). Similarly, the scale factor is given by

$$\xi(l) \equiv \begin{cases} 1/2 & l = 1 \\ 1 & l \neq 1, \end{cases} \quad (2.16)$$

while

$$\tau_1 = y_1'(b; l) + \left(\frac{b}{\sqrt{1-b^2}} - i\lambda\Lambda \right) y_1(b; l), \quad \tau_2 = y_2'(b; l) + \left(\frac{b}{\sqrt{1-b^2}} - i\lambda\Lambda \right) y_2(b; l). \quad (2.17)$$

Note that the Green's function is parameterized by azimuthal wavenumber l , forcing frequency λ and contact-line mobility Λ .

2.3.1. Spectral reduction

A solution series

$$\phi = \sum_{j=1}^N a_j \phi_j, \quad (2.18)$$

is applied to (2.13) and inner products are taken to generate a set of algebraic equations

$$\sum_{j=1}^N (m_{ij} + i\epsilon\lambda\tau_{ij} - \lambda^2\kappa_{ij}) a_j = F_0\lambda\gamma_i, \quad (2.19)$$

with

$$\begin{aligned} m_{ij} &\equiv (1-b^2) \int_b^1 \frac{\partial \phi_i}{\partial n} \phi_j dx, \quad \tau_{ij} \equiv \int_b^1 \int_b^1 G(x, t) (\hat{n} \cdot (\nabla \otimes \nabla \phi_i) \cdot \hat{n}) \phi_j(x) dx dt, \\ \kappa_{ij} &\equiv \int_b^1 \int_b^1 G(x, t) \phi_i(t) \phi_j(x) dx dt, \quad \gamma_i \equiv \int_b^1 \int_b^1 G(x, t) \phi_i(x) dx dt. \end{aligned} \quad (2.20)$$

The auxiliary conditions (2.12) are satisfied through proper selection of the basis functions ϕ_j , as discussed in Bostwick & Steen (2014, §4.2). For zonal modes,

$$\phi_j(\rho, \theta) = \rho^{2j} P_{2j}(\cos \theta), \quad (2.21)$$

while for non-zonal modes,

$$\phi_j^{(l)}(\rho, \theta) = \rho^j P_j^{(l)}(\cos \theta) \quad (2.22)$$

with $j+l = \text{even}$.

3. Results

For fixed $\lambda, \epsilon, \alpha, l$, we compute the solution a_j to the matrix equation (2.19). The associated fluid response $\phi, \partial\phi/\partial n$ is then obtained by applying a_j to (2.18). Modal identities

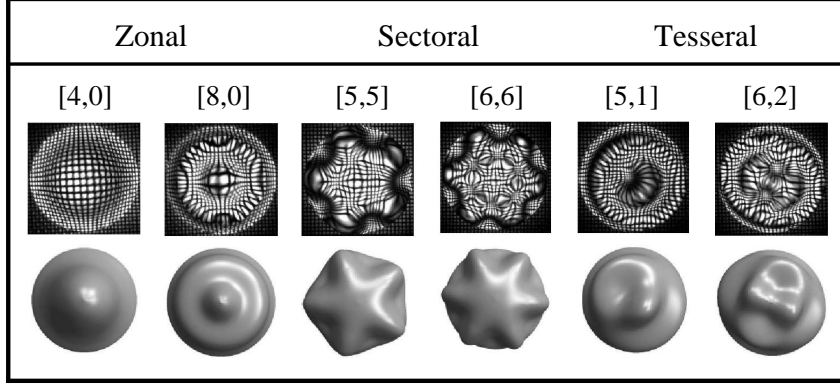


FIGURE 2. Modal classification by wavenumber pair $[k, l]$ into zonal $[k, 0]$, sectoral $[k, k]$ and tesseral $[k, l \neq k]$ shapes. Experimental images are reproduced from Part 2 (Chang *et al.* 2015).

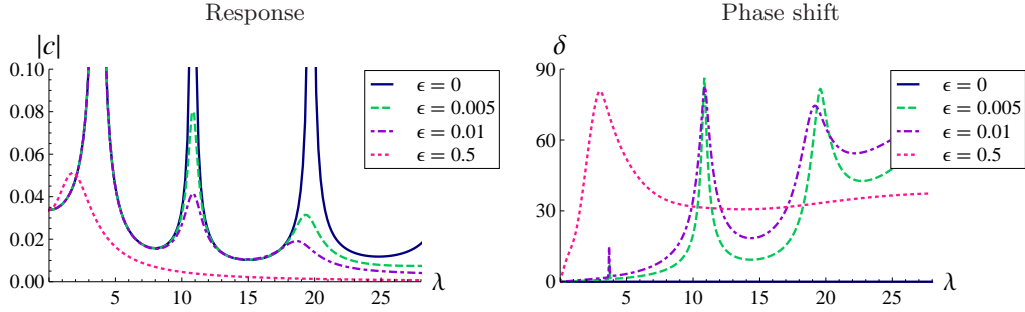


FIGURE 3. Response $|c|$ (left) and phase shift δ (right) against frequency λ for a drop with $\alpha = 75^\circ$, $\Lambda = 0$ (fully-mobile disturbance) and $l = 0$, as it depends upon the Ohnesorge number ϵ . The first peak corresponds to the $[2, 0]$ mode, the second to $[4, 0]$ and the third to $[6, 0]$. Note for inviscid fluids $\epsilon = 0$, the phase shift $\delta = 0^\circ$ for all α .

are distinguished by the wavenumber pair $[k, l]$ that follow the spherical harmonic classification scheme; zonal $[k, 0]$, sectoral $[k, k]$ and tesseral $[k, l \neq k]$ shapes, as shown in Figure 2. An alternate identification uses layers and sectors (Chang *et al.* 2015). The focus here is the droplet response a_j , which is linear in the applied pressure amplitude F_0 . Henceforth, we report the complex response as $c_j \equiv a_j/F_0$, which admits a phase shift

$$\delta = \arctan \left| \frac{\text{Im}[c]}{\text{Re}[c]} \right|. \quad (3.1)$$

For $\delta = 0^\circ$ and $\delta = 90^\circ$, the droplet response is in-phase and out-of-phase with the applied pressure oscillations, respectively, with $\delta = 90^\circ$ corresponding to a state of maximal dissipation. Note the damped-driven oscillator structure of (2.19) with corresponding features. In what follows, we show how the response diagram changes with viscosity ϵ and contact-line mobility Λ and compare against relevant experiments when appropriate.

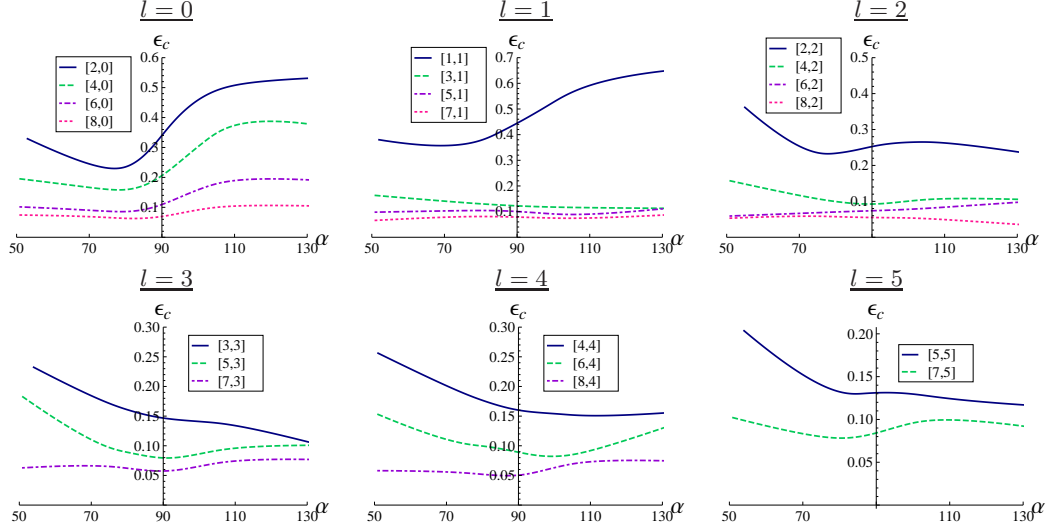


FIGURE 4. Critical Ohnesorge number ϵ_c against contact-angle α for pinned disturbances $\Lambda = \infty$. Mode $[k, l]$ can be excited below the corresponding curve. Note the different vertical scales between sub-figures.

3.1. Viscosity ϵ

Figure 3 plots the droplet response and phase shift for the zonal modes for a sub-hemispherical drop ($\alpha = 75^\circ$) with $\Lambda = 0$, as they depend upon the bulk viscosity ϵ . For an inviscid fluid $\epsilon = 0$, the oscillations are completely in phase $\delta = 0^\circ$ with the applied field and the response diagram exhibits three infinite peaks that correspond to the $[2, 0]$, $[4, 0]$ and $[6, 0]$ modes, respectively. Note that modes appear over a range of frequencies that define a bandwidth, a prominent feature of the forced oscillation problem that is also observed in experiment (Chang *et al.* 2015). For small viscosity $\epsilon = 0.01$, the resonance peaks are dramatically lowered and the droplet response is out of phase $\delta \neq 0^\circ$ with the driving frequency. The relative decrease in response amplitude $|c|$ for increasing wavenumber is consistent with bulk viscous effects leading to traditional viscous dissipation (Lamb 1932).

Resonance peaks may disappear completely for large values of viscosity, as shown in Figure 3 for the $[4, 0]$ and $[6, 0]$ modes with $\epsilon = 0.5$. For a given mode $[k, l]$, one can define a critical Ohnesorge number ϵ_c where the resonance peak disappears and above which ($\epsilon > \epsilon_c$) it is not possible to excite that mode. Stated differently, beyond ϵ_c the oscillations are over-damped. Figure 4 plots ϵ_c against contact angle for the pinned $\Lambda = \infty$ modes. Note that for a fixed azimuthal wavenumber l , ϵ_c decreases with increasing polar wavenumber k irrespective of contact-angle, as could be expected from the increased surface distortion for the high wavenumber modes (Chang *et al.* 2015, Fig. 7). However, the non-monotonic behavior with contact angle α could not have been predicted a priori and presumably results from the interactions between adjacent modes and the applied pressure field.

A typical measure of the damping of oscillations in forced systems is the bandwidth of a resonance peak, which can easily be extracted from the response diagram (e.g. Figure 3). In particular, the full width at half max (FWHM) bandwidth also coincides with the decay rate of oscillations (Sharp 2012). Figure 5(a) plots the dimensionless FWHM $\Delta\lambda$ against ϵ and α for the $[1, 1]$ pinned mode. Note the non-monotonic dependence of the

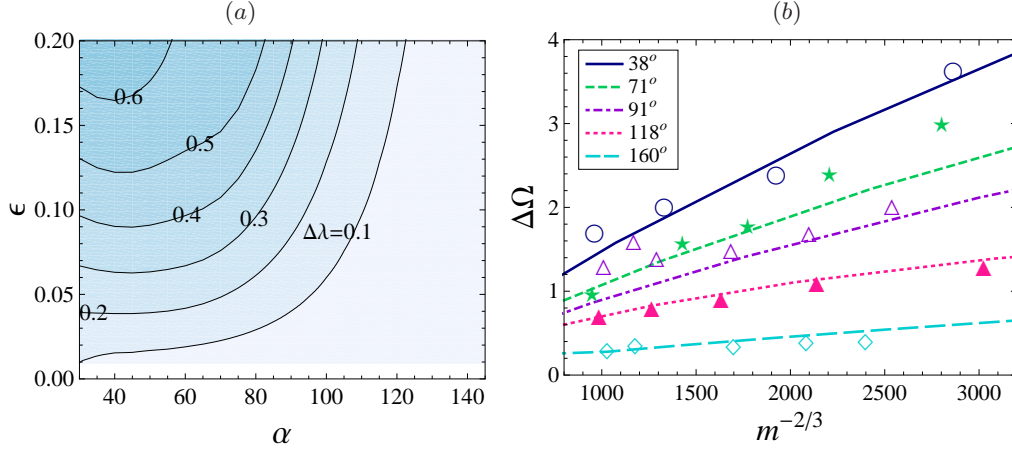


FIGURE 5. Full width at half max (FWHM) for the $[1, 1]$ pinned mode: (a) dimensionless frequency $\Delta\lambda$ against Ohnesorge number ϵ and contact-angle α and (b) dimensional frequency $\Delta\Omega$ against $1/m^{2/3}$ for 10%w glycerol droplets comparing to Sharp (2012) (symbols).

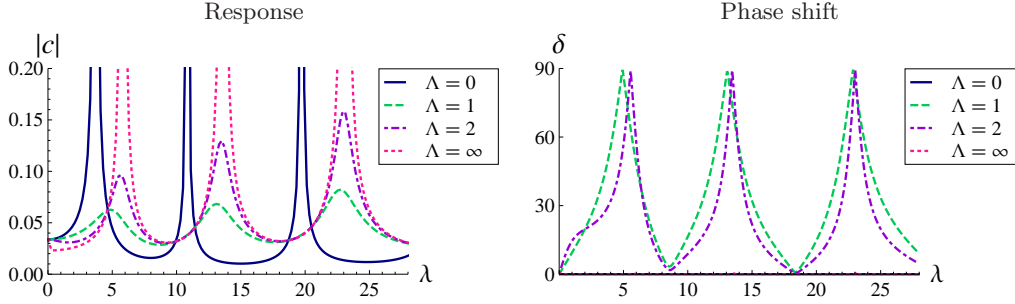


FIGURE 6. Response $|c|$ (left) and phase shift δ (right) against frequency λ for the zonal $l = 0$ modes of an inviscid $\epsilon = 0$ drop with $\alpha = 75^\circ$, as it depends upon the mobility Λ . The first peak corresponds to the $[2, 0]$ mode, the second to $[4, 0]$ and the third to $[6, 0]$. Note that the response is strictly real with phase shift $\delta = 0^\circ$ for the free $\Lambda = 0$ and pinned $\Lambda = \infty$ disturbances (superposed lines on λ axis). For finite mobility Λ , the drop response is out-of-phase $\delta = 90^\circ$ at the resonant peak.

dissipation (FWHM) with respect to contact angle, reflecting the increased presence of the solid substrate for these wetting conditions. We compare our FWHM bandwidth predictions $\Delta\Omega$ for the $[1, 1]$ pinned mode to the experiments by Sharp (2012) over a wide range of contact angles in Figure 5(b). The agreement is reasonable over a large range of drop volumes, as measured by the drop mass m , suggesting the relevance of our theory to the given experiments.

3.2. CL mobility Λ

We examine the role of contact-line mobility by plotting the response diagram and phase shift for the zonal $l = 0$ modes for an inviscid $\epsilon = 0$ drop with $\alpha = 75^\circ$ in Figure 6 for various values of Λ . We set $\epsilon = 0$ to eliminate the effects of bulk viscous dissipation. For fully-mobile $\Lambda = 0$ and pinned $\Lambda = \infty$ disturbances, the respective resonance peaks are infinite and the droplet oscillates in phase $\delta = 0^\circ$ with the forcing frequency. However, for finite values of Λ the resonance peak becomes finite and the oscillations become out-of-phase with the driving field, indicating that finite contact-line mobility Λ leads

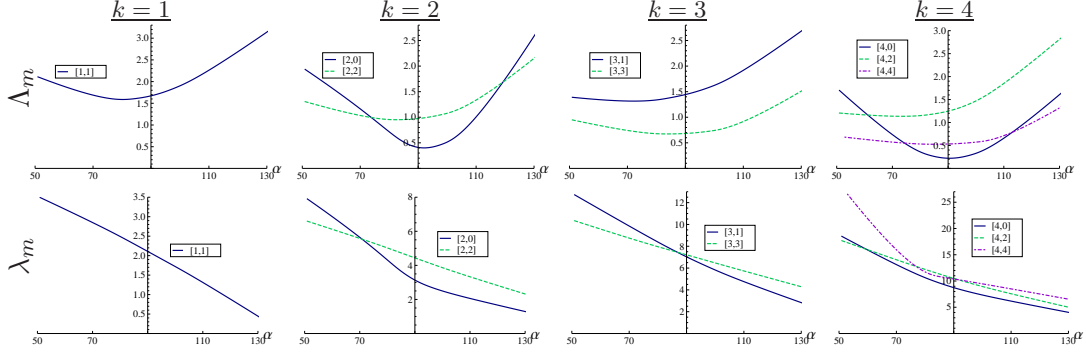


FIGURE 7. Critical mobility Λ_m and critical frequency λ_m that generates the largest Davis dissipation for fixed polar wavenumber k , as it depends upon the contact-angle α and azimuthal wavenumber l . Viscous effects are negligible $\epsilon = 0$. Note the different vertical scales between sub-figures.

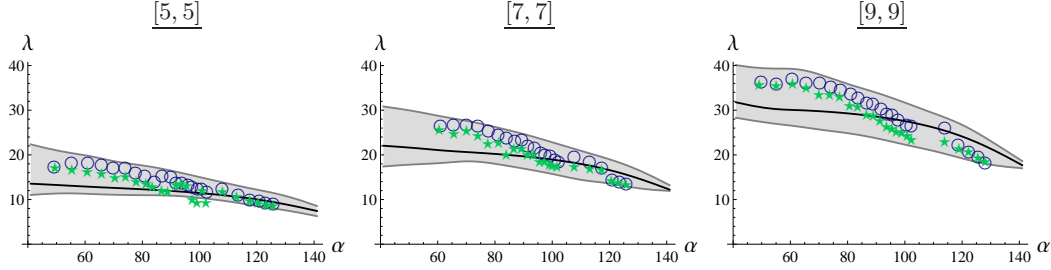


FIGURE 8. Comparison with Chang *et al.* (2015) experiments: frequency envelopes against contact-angle α for sectoral modes $[5, 5]$, $[7, 7]$, $[9, 9]$ with contact-line mobility $\Lambda = 0.1$ and $\epsilon = 0.0024$. Experiments given by symbols.

to an effective dissipation. Bostwick & Steen (2015) have deemed this feature ‘Davis dissipation’ since it can be traced back to the work of Davis (1980) on fluid rivulets. Note that the resonance peaks become larger for increasing polar wavenumber k , indicating that the low order modes dissipate the most energy for fixed Λ . This feature is consistent with the results of Bostwick & Steen (2014, Fig. 13), who showed that for fixed azimuthal wavenumber l the lower wavenumber k modes have the largest contact-line excursion leading to increased Davis dissipation.

For the mobility Λ_m , the resonance peak will be smallest and the droplet response is minimal. We call Λ_m the critical mobility and λ_m the critical frequency that generates the largest Davis dissipation. Figure 7 plots Λ_m, λ_m against contact-angle α for the $k = 1 - 4$ modes. The forcing frequency λ_m monotonically decreases with increasing contact angle, while the mobility Λ_m is more complex. For example, the zonal modes $[2, 0], [4, 0]$ can have the smallest or largest critical mobility, for fixed polar wavenumber k , depending upon the contact angle. An important aspect of this study is the damping of oscillations for inviscid ($\epsilon = 0$) fluids. Figure 7 may be interpreted as a guide in selecting substrates for experiments that generate the largest Davis dissipation.

The response diagrams of Figures 3,6, show that modes can be excited over a range of forcing frequencies. This has been observed in recent experiments for a number of modes and over a range of contact angles (Chang *et al.* 2015). In that study, predicted frequency envelopes for pinned ($\Lambda = \infty$) disturbances with $\epsilon = 0.0024$ compared favorably to experiment for a large number of modes, with the exception of the $[5, 5]$, $[7, 7]$, $[9, 9]$ sectoral

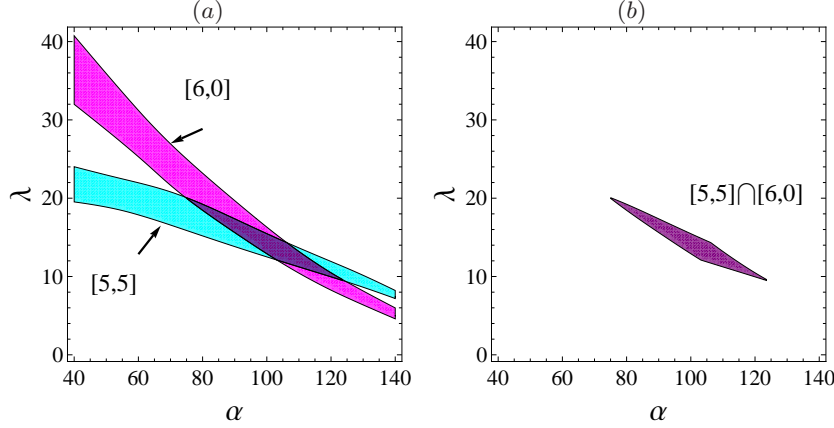


FIGURE 9. Modal coexistence: (a) frequency λ envelopes for the pinned ($\Lambda = \infty$) $[6, 0]$ and $[5, 5]$ modes against contact-angle α predicts (b) domains of coexistence for a drop with $\epsilon = 0.0024$.

modes. By taking account of the contact-line mobility $\Lambda = 0.1$, we are able to predict frequency envelopes that match the experiments for those remaining modes, suggesting that the contact-line dynamics are crucial in understanding the forced oscillations problem (c.f. Figure 8).

3.3. Modal coexistence

An important prediction from Part 1 was that two modes with different wavenumber pair $[k, l]$ may share the same natural frequency and that the classical ordering of frequencies by increasing polar wavenumber could become broken and disordered for certain contact angles. This was confirmed in the experiments by Chang *et al.* (2015), who also showed that the appearance of a dominant mode in regions where two modes may coexist is hysteretic. That is, the observed mode depends upon the direction of the frequency sweep.

A primary difference between natural and forced oscillations is that the resonance frequency takes a discrete value for the former and a range of values for the latter. Hence, two modes may coexist over a range of frequencies for the forced problem considered here. Figure 9(a) plots the frequency envelopes for the pinned $[6, 0]$ zonal and $[5, 5]$ sectoral modes against contact angle α for the Ohnesorge number $\epsilon = 0.0024$ used in the Chang *et al.* (2015) experiments. Modal coexistence is predicted in the region shown in Figure 9(b). In general, the domains of coexistence for a pair of modes will depend upon both the contact-line mobility Λ and the Ohnesorge number ϵ . Figure 10 plots the domains of coexistence for a given zonal mode with the sectoral modes, comparing pinned $\Lambda = \infty$ disturbances to those with finite mobility $\Lambda = 0.1$. As shown, decreasing Λ tends to increase the number of modes that coexist with a given target mode. Figure 10 can be used as a guide to future studies of modal interactions both theoretically and experimentally. For reference, we include additional Figures 11, 12, 13 that predict domains of coexistence for different target modes in the Appendix.

4. Concluding remarks

We have studied the forced oscillations of a partially-wetting sessile drop, whose three-phase contact line obeys a constitutive law relating the contact angle to the contact line speed, sometimes called the Hocking condition. Response diagrams and phase shifts

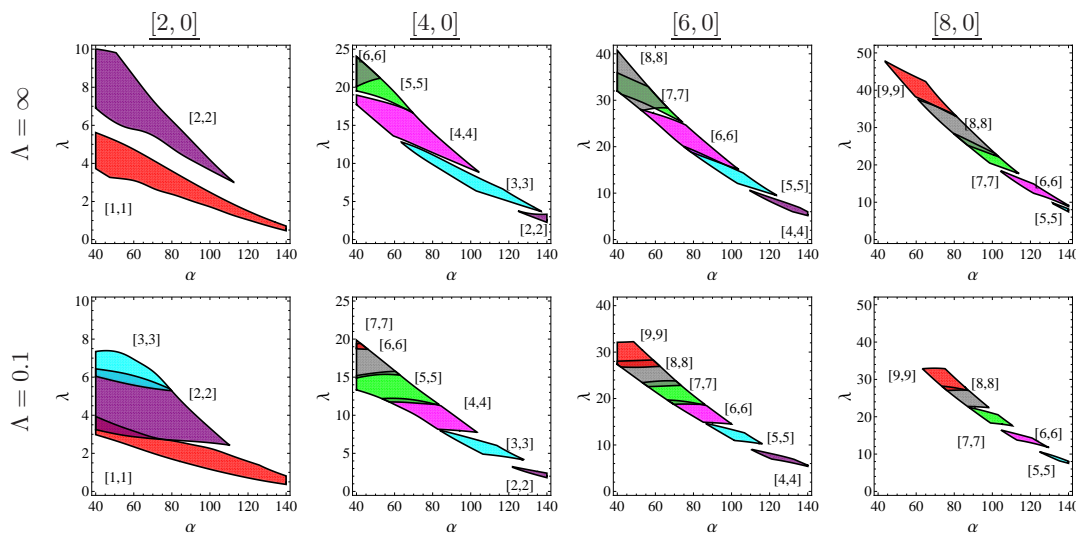


FIGURE 10. Domains of coexistence for the zonal modes $[k, 0]$ mixed with the sectoral modes $[k, k]$ for pinned $\Lambda = \infty$ and finite contact-line mobility $\Lambda = 0.1$ disturbances with $\epsilon = 0.0024$. Note the different frequency scales between sub-figures.

are reported, as they depend upon viscosity ϵ and contact line mobility Λ . Modes are distinguished by the wavenumber pair $[k, l]$ and can be excited over a range of frequencies that define a bandwidth. Our predictions compare well against relevant experiments on vibrated sessile drops (c.f. Figures 5(b), 8), suggesting the predictive nature of our model.

Our focus is on defining regimes or ‘operating windows’ where certain droplet behavior may be observed experimentally or our model developed further. For example, we compute the critical viscosity ϵ_c (Ohnesorge number) above which it is not possible to observe a specified mode over a range of contact angles, thereby aiding the practitioner in selecting appropriate fluids and droplet volumes (c.f. Figure 4). We then show how finite contact line mobility Λ leads to Davis dissipation, even in inviscid fluids, and compute the critical mobility Λ_m and forcing frequency λ_m that generate the largest dissipation (c.f. Figure 7). Finally, we show that two distinct modes may be simultaneously excited by a single forcing frequency and map these regions of modal coexistence in parameter space for a number of modal pairs in Figure 10. Modal coexistence may be of importance in mixing applications that rely upon capillary oscillations (Mugele *et al.* 2006; Mampallil *et al.* 2011; Davoust *et al.* 2013) and drop atomization (Tsai *et al.* 2012; Vukasinovic *et al.* 2007) for spray cooling. With regard to modeling, a thorough study of the internal resonances and nonlinear modal interactions (Natarajan & Brown 1987; Henderson & Miles 1991) in the coexistence domains would help identify the mechanism behind mode selection in related experiments (Chang *et al.* 2015).

REFERENCES

- BASARAN, O. & DEPAOLI, D. 1994 Nonlinear oscillations of pendant drops. *Phys. Fluids* **6**, 2923–2943.
- BASARAN, OSMAN A, GAO, HAIJING & BHAT, PRADEEP P 2013 Nonstandard inkjets. *Annual Review of Fluid Mechanics* **45**, 85–113.
- BAUDOIN, MICHAEL, BRUNET, PHILIPPE, BOU MATAR, OLIVIER & HERTH, ETIENNE 2012 Low power sessile droplets actuation via modulated surface acoustic waves. *Applied Physics Letters* **100** (15), 154102.

- BENJAMIN, T. B. & URSELL, F. 1954 The stability of the plane free surface of a liquid in vertical periodic motion. *Proceedings of the Royal Society of London. Series A. Mathematical and Physical Sciences* **225** (1163), 505–515.
- BOSTWICK, J.B. & STEEN, P.H. 2009 Capillary oscillations of a constrained liquid drop. *Phys. Fluids* **21**, 032108.
- BOSTWICK, J.B. & STEEN, P.H. 2013a Coupled oscillations of deformable spherical-cap droplets. part 1. inviscid motions. *J. Fluid Mech.* **714**, 312–335.
- BOSTWICK, J.B. & STEEN, P.H. 2013b Coupled oscillations of deformable spherical-cap droplets. part 2. viscous motions. *J. Fluid Mech.* **714**, 336–360.
- BOSTWICK, J.B. & STEEN, P.H. 2014 Dynamics of sessile drops. part 1. inviscid theory. *J. Fluid Mech.* **760**, 5–38.
- BOSTWICK, J.B. & STEEN, P.H. 2015 Stability of constrained capillary surfaces. *Ann. Rev. Fluid Mech.* **47**, 539–568.
- BRUNET, P., EGGERS, J & DEEGAN, RD 2007 Vibration-induced climbing of drops. *Physical review letters* **99** (14), 144501.
- CALVERT, PAUL 2001 Inkjet printing for materials and devices. *Chemistry of materials* **13** (10), 3299–3305.
- CASTREJON-PITA, J. RAFAEL, BAXTER, W. R. S., MORGAN, J., TEMPLE, S., MARTIN, G. D. & HUTCHINGS, I. M. 2013 Future, opportunities and challenges of inkjet technologies. *Atomization and Sprays* **23** (6), 541–565.
- CHANDRASEKHAR, S. 1961 *Hydrodynamic and Hydromagnetic Stability*. Oxford: Oxford University Press.
- CHANG, C.T., BOSTWICK, J.B., DANIEL, S. & STEEN, P.H. 2015 Dynamics of sessile drops. part 2. experiment. *J. Fluid Mech.* **768**, 442–467.
- CHANG, C.T., BOSTWICK, J.B., STEEN, P.H. & DANIEL, S. 2013 Substrate constraint modifies the rayleigh spectrum of vibrating sessile drops. *Phys. Rev. E* **88**, 023015.
- CHEBEL, NICOLAS ABI, RISSO, FRDRIK & MASBERNAT, OLIVIER 2011 Inertial modes of a periodically forced buoyant drop attached to a capillary. *Phys. Fluids* **23** (10), 102104.
- DAVIS, S.H. 1980 Moving contact lines and rivulet instabilities. part 1. the static rivulet. *J. Fluid Mechanics* **98**, 225–242.
- DAVOUST, LAURENT, FOUILLET, YVES, MALK, RACHID & THEISEN, JOHANNES 2013 Coplanar electrowetting-induced stirring as a tool to manipulate biological samples in lubricated digital microfluidics. impact of ambient phase on drop internal flow pattern). *Biomicrofluidics* **7** (4), 044104.
- DEEPU, P, BASU, SAPTARSHI & KUMAR, RANGANATHAN 2014 Multimodal shape oscillations of droplets excited by an air stream. *Chemical Engineering Science* **114**, 85–93.
- DONNELLY, THOMAS D, HOGAN, J, MUGLER, A, SCHOMMER, N, SCHUBMEHL, M, BERNOFF, ANDREW J & FORREST, B 2004 An experimental study of micron-scale droplet aerosols produced via ultrasonic atomization. *Physics of Fluids* **16** (8), 2843–2851.
- GRIMM, T. 2004 *User's Guide to Rapid Prototyping*. Society of Manufacturing Engineers.
- HENDERSON, DIANE M & MILES, JOHN W 1991 Faraday waves in 2: 1 internal resonance. *Journal of Fluid Mechanics* **222**, 449–470.
- HOCKING, L.M. 1987 The damping of capillary-gravity waves at a rigid boundary. *J. Fluid Mech.* **179**, 253–266.
- JOSEPH, D.D. 2006 Helmholtz decomposition coupling rotational to irrotational flow of a viscous fluid. *PNAS* **103**, 14272–14277.
- KIM, JUNGHO 2007 Spray cooling heat transfer: the state of the art. *International Journal of Heat and Fluid Flow* **28** (4), 753–767.
- KREYSZIG, E. 1991 *Differential Geometry*. New York, NY: Dover Publications.
- LAMB, H. 1932 *Hydrodynamics*. Cambridge: Cambridge University Press.
- LUNDGREN, T.S. & MANSOUR, N.N. 1988 Oscillations of drops in zero gravity with weak viscous effects. *J. Fluid Mech.* **194**, 479–510.
- LYUBIMOV, D.V., LYUBIMOVA, T.P. & SHKLYAEV, S.V. 2004 Non-axisymmetric oscillations of a hemispheric drop. *Fluid Dyn.* **39**, 851.
- LYUBIMOV, D.V., LYUBIMOVA, T.P. & SHKLYAEV, S.V. 2006 Behavior of a drop on an oscillating solid plate. *Phys. Fluids* **18**, 012101.
- MACROBERT, T.M. 1967 *Spherical Harmonics*. New York, NY: Pergamon.

- MAMPALLIL, DILEEP, VAN DEN ENDE, DIRK & MUGELE, FRIEDER 2011 Controlling flow patterns in oscillating sessile drops by breaking azimuthal symmetry. *Applied Physics Letters* **99** (15), 154102.
- MAMPALLIL, DILEEP, ERAL, H BURAK, STAICU, ADRIAN, MUGELE, FRIEDER & VAN DEN ENDE, DIRK 2013 Electrowetting-driven oscillating drops sandwiched between two substrates. *Physical Review E* **88** (5), 053015.
- MILLER, C.A. & SCRIVEN, L.E. 1968 The oscillations of a fluid droplet immersed in another fluid. *J. Fluid Mech.* **32**, 417–435.
- MUGELE, F, BARET, J-C & STEINHAUSER, D 2006 Microfluidic mixing through electrowetting-induced droplet oscillations. *Applied Physics Letters* **88** (20), 204106–204106.
- NATARAJAN, RAMESH & BROWN, ROBERT A 1987 Third-order resonance effects and the non-linear stability of drop oscillations. *Journal of Fluid Mechanics* **183**, 95–121.
- NOBLIN, X, BUGUIN, A & BROCHARD-WYART, F 2004 Vibrated sessile drops: Transition between pinned and mobile contact line oscillations. *The European Physical Journal E: Soft Matter and Biological Physics* **14** (4), 395–404.
- NOBLIN, X., BUGUIN, A. & BROCHARD-WYART, F. 2005 Triplon modes of puddles. *Phys. Rev. Letters* **94**, 166102.
- NOBLIN, XAVIER, KOFMAN, RICHARD & CELESTINI, FRANCK 2009 Ratchetlike motion of a shaken drop. *Physical review letters* **102** (19), 194504.
- PADRINO, J.C., FUNADA, T. & JOSEPH, D.D. 2007 Purely irrotational theories for the viscous effects on the oscillations of drops and bubbles. *International Journal of Multiphase Flow* **34**, 61–75.
- PARK, Y.B., IM, H., M.IM & CHOI, Y.K. 2011 Self-cleaning effect of highly water-repellent microshell structures for solar cell applications. *J. Mater. Chem.* **21**, 633–636.
- PROSPERETTI, A. 1980 Normal-mode analysis for the oscillations of a viscous liquid drop in an immiscible liquid. *J. Mecanique* **19**, 149–182.
- RAMALINGAM, S.K. & BASARAN, O.A. 2010 Axisymmetric oscillation modes of a double droplet system. *Phys. Fluids* **22**, 112111.
- RAYLEIGH, LORD 1879 On the capillary phenomenon of jets. *Proc. R. Soc. Lond.* **29**, 71–97.
- REID, W.H. 1960 The oscillations of a viscous liquid drop. *Q. Appl. Math.* **18**, 86–89.
- SHARP, J.S. 2012 Resonant properties of sessile droplets; contact angle dependence of the resonant frequency and width in glycerol/water mixtures. *Soft Matter* **8**, 399–407.
- SHARP, J.S., FARMER, D.J. & KELLY, J. 2011 Contact angle dependence of the resonant frequency of sessile water droplets. *Langmuir* **27** (15), 9367–9371.
- STONE, H.A., STROOCK, A.D. & AJDARI, A. 2004 Engineering flows in small devices: Microfluidics toward a lab-on-a-chip. *Annual Review of Fluid Mechanics* **36**, 381411.
- STRANI, M. & SABETTA, F. 1984 Free vibrations of a drop in partial contact with a solid support. *J. Fluid Mech.* **141**, 233.
- TILGER, CHRISTOPHER F, OLLES, JOSEPH D & HIRSA, AMIR H 2013 Phase behavior of oscillating double droplets. *Applied Physics Letters* **103** (26), 264105.
- TRINH, E. & WANG, T.G. 1982 Large-amplitude free and driven drop-shape oscillation: experimental results. *J. Fluid Mech.* **122**, 315–338.
- TSAI, SHIRLEY C, LIN, SHIH K, MAO, RONG W & TSAI, CHEN S 2012 Ejection of uniform micrometer-sized droplets from faraday waves on a millimeter-sized water drop. *Physical review letters* **108** (15), 154501.
- TSAMOPOULOS, J.A. & BROWN, R.A. 1983 Nonlinear oscillations of inviscid drops and bubbles. *J. Fluid Mech.* **127**, 519–537.
- VUKASINOVIC, B., SMITH, M.K. & GLEZER, A. 2007 Dynamics of a sessile drop in forced vibration. *J. Fluid Mech.* **587**, 395–423.
- WANG, T.G., ANILKUMAR, A.V. & LEE, C.P. 1996 Oscillations of liquid drops : results from usml-1 experiments in space. *J. Fluid Mech.* **308**, 1–14.

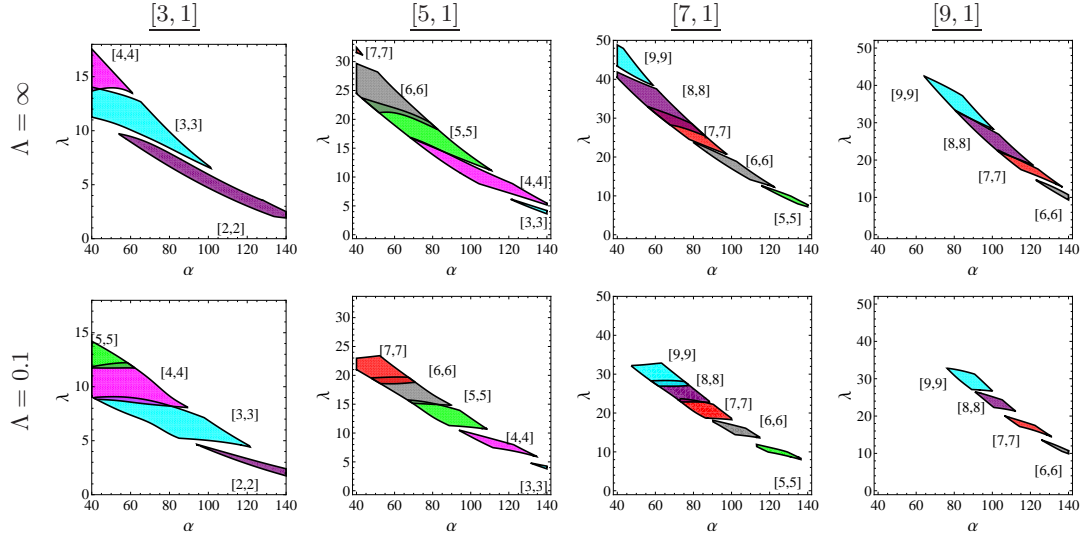


FIGURE 11. Domains of coexistence for the rocking modes $[k, 1]$ mixed with the sectoral modes $[k, k]$ for pinned $\Lambda = \infty$ and finite contact-line mobility $\Lambda = 0.1$ disturbances with $\epsilon = 0.0024$.

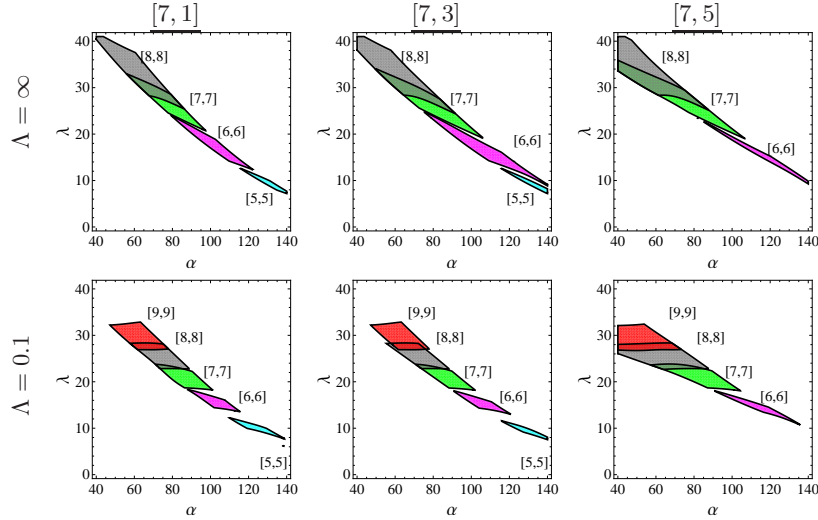


FIGURE 12. Domains of coexistence for the $[7, l]$ modes mixed with the sectoral modes $[k, k]$ for pinned $\Lambda = \infty$ and finite contact-line mobility $\Lambda = 0.1$ disturbances with $\epsilon = 0.0024$.

Appendix A. Modal coexistence domains

Figures 11, 12 & 13 map the regions of modal coexistence for the $l = 1, k = 7, k = 8$ modes with the sectoral modes for pinned $\Lambda = \infty$ and finite mobility $\Lambda = 0.1$ disturbances.

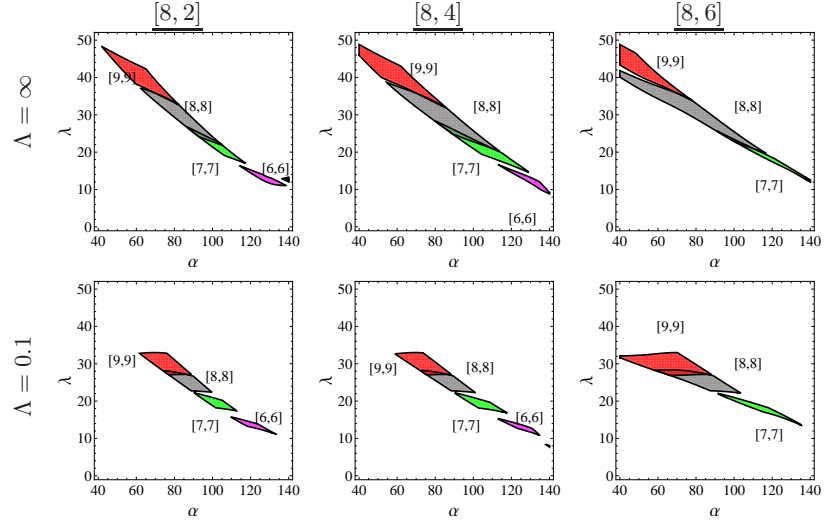


FIGURE 13. Domains of coexistence for the $[8, l]$ modes mixed with the sectoral modes $[k, k]$ for pinned $\Lambda = \infty$ and finite contact-line mobility $\Lambda = 0.1$ disturbances with $\epsilon = 0.0024$.